Journal of Materials Chemistry A

ROYAL SOCIETY OF CHEMISTRY

PAPER

View Article Online
View Journal

Cite this: DOI: 10.1039/d5ta00677e

Hybrid central substitution of acceptors boosts the efficiency of near-infrared organic photovoltaics†

Yu Li,‡[a] Xinyuan Jia,‡[a] Xingqi Bi,‡[a] Kaiyuan Wang,[c] Wenkai Zhao,[d] Xiangjian Cao,[a] Zhaoyang Yao,*[a] Yaxiao Guo,[b] Zhenjie Zhang,[c] Guankui Long,[d] Chenxi Li,[a] Xiangjian Wan[a] and Yongsheng Chen*[a]

Received 7th February 2025
Accepted 14th March 2025

DOI: 10.1039/d5ta00677e

rsc.li/materials-a

Near-infrared (NIR) organic photovoltaic molecules are usually restricted by the "energy-gap law", making it greatly challenging to simultaneously achieve organic solar cells (OSCs) with a high open-circuit voltage (V_{OC}) and NIR absorption. Herein, a synergistic strategy involving the hybrid central substitution on acceptors with an electron-donating methyl/methoxy group was developed, allowing NIR absorption with the electron-withdrawing bromine inducing favorable molecular packing. Single-crystal analysis revealed the rarely observed OC–H···S non-covalent interaction and potentially beneficial entanglement of alkyl chains in CH29 with a central methoxy group. Consequently, an OSC fabricated with CH29 achieved an excellent V_{OC} of 884 mV and a short-circuit current density of 28.30 mA cm^{-2} under a quite narrow optical bandgap of ≈1.33 eV while showing an almost minimal energy loss. Our successful attempt at hybrid central substitution provides a feasible pathway to construct high-performance NIR acceptors, which are essential to obtaining record-breaking OSCs, especially for the rear cells of tandem devices that simultaneously require high V_{OC} and a broad photoelectric response.

Introduction

Benefitting from the unremitting innovation of novel small molecular acceptors (SMAs),[1,2] organic solar cells (OSCs) with an amazing power conversion efficiency (PCE) exceeding 20% have been developed.[3–13] Among the multiple factors that determine the photoelectric characteristics of SMAs, such as the frontier orbital energy level alignment, molecular planarity and packing behavior, a delicately tuned absorption that is more consistent with the solar spectrum carries great significance.[14–19] However, near-infrared (NIR) organic molecules are typically constrained by the "energy-gap law",[20] which results in severe non-radiative recombination in organic photovoltaic devices by intensifying the exciton-vibration coupling or electron-vibration coupling between the charge transfer (CT) and ground states.[21–23] This insurmountable challenge confronted by NIR-SMAs limits the simultaneous achievement of a small bandgap and large open-circuit voltage (V_{OC}) in OSCs.[24–26]

In view of harvesting sufficient low-energy photons from sunlight, the exploration of high-performance NIR-SMAs is quite essential, particularly considering the great success of commercial silicon cells with absorption of up to 1100 nm.[27] Furthermore, NIR-SMAs are expected to enable champion tandem devices by means of reducing transmission and thermalization losses in single-junction OSCs.[28–35] Currently, the emergence of Y-series SMAs has provided a new opportunity to develop high-performance NIR-SMAs that can overcome the constraints of the "energy-gap law" to some extent.[2] The breakthrough point may lie in the more compact and ordered three-dimensional (3D) molecular packing network of SMAs, which could efficiently delocalize the vibration of photo-generated excitons on neighboring stacked molecules, thus weakening the coupling between the molecular excited and ground states.[14,36–38] It is worth noting that these advantages could be greatly amplified if we could further strengthen the intermolecular interactions of SMAs by extending their central units to two dimensions (such as CH6 and CH22).[15,39] More importantly, the additional active sites on such two-dimensional (2D) central units make it possible to regulate

[a]State Key Laboratory and Institute of Elemento-Organic Chemistry, The Centre of Nanoscale Science and Technology and Key Laboratory of Functional Polymer Materials, Renewable Energy Conversion and Storage Center (RECAST), College of Chemistry, Nankai University, Tianjin, 300071, China. E-mail: yschen99@nankai.edu.cn; zyao@nankai.edu.cn

[b]State Key Laboratory of Separation Membranes and Membrane Processes, School of Chemistry, Tiangong University, Tianjin 300387, China

[c]State Key Laboratory of Medicine Chemistry Biology, College of Chemistry, Nankai University, Tianjin 300071, China

[d]School of Materials Science and Engineering, National Institute for Advanced Materials, Renewable Energy Conversion and Storage Center (RECAST), Nankai University, Tianjin, 300350, China

† Electronic supplementary information (ESI) available. CCDC 2386133 and 2386134. For ESI and crystallographic data in CIF or other electronic format see DOI: https://doi.org/10.1039/d5ta00677e

‡ These authors contributed equally.

the absorption of SMAs by means of simple central substitution rather than requiring the structural reconstruction of S, N-heteroacene.[39–42]

Herein, we developed a hybrid central substitution strategy, with the aim of further boosting the absorption of SMAs towards the NIR region while maintaining the desired molecular crystallinity and packing. Specifically, on the basis of a high-performance molecular skeleton of CH22, a moderate or strong electron-donating group (methyl or methoxy) was incorporated into one active site on the central unit, while the inclusion of a bromine atom at another position promoted ordered molecular packing, leading to an improved crystallinity of the active layer (Fig. 1a). This approach allowed the electron-donating methyl or methoxy group to extend the absorption of SMAs towards the NIR region, while Br inclusion induced a favorable molecular packing and film morphology, thereby achieving a good balance between NIR absorption and the desired molecular crystallinity. By maximizing the advantages of methoxy and bromine, an OSC based on CH29 achieved an excellent PCE of 19.12%, along with the highest V_{OC} (884 mV) reported to date for materials with comparable bandgaps.[2,43] A systematic analysis, including single-crystal and nanoscale morphology analyses, underscored the significant potential of hybrid central substitution for constructing NIR acceptors. These advances are particularly crucial for the future integration of NIR-OSCs into tandem solar cells, in which high efficiency, large V_{OC} and broad spectral absorption are essential.[44,45]

Results and discussions

Fig. 1a and Scheme S1† display the chemical structures of the three SMAs and their synthetic routes, respectively. Due to the nearly identical molecular backbones of CH22, CH28 and CH29, it could be observed that they had similar planar configurations and frontier molecular orbital distributions (Fig. S1†). With respect to the Br atom, the methyl and methoxy groups exhibited a distinctive electron-donating feature according to the ESP maps (Fig. S2†). Therefore, the highest occupied molecular orbital (HOMO) energy levels of CH28 and CH29 were greatly upshifted by ≈90 meV, resulting in a decreased bandgap of ≈2.02 eV for both CH28 and CH29 compared with that of ≈2.04 eV for CH22 (Fig. 1b). All three SMAs exhibited a clear acceptor–donor–acceptor (A–D–A) characteristic (Fig. 1c), which has been proven to render superior charge-transfer/transport capabilities in the resulting OSCs.[2,46–48] As indicated by the peaks and valleys that swayed and fluctuated along the molecular skeletons (Fig. 1c), the electron-donating and withdrawing centers of CH28 and CH29 deviated from those of CH22. Therefore, the dipole direction of unsymmetrical CH28 and CH29 became almost parallel to the longest molecular skeleton, rather than perpendicular to that in CH22 (Fig. S2†). This change in dipole moment was likely caused by the hybrid central substitution and would enhance electron migration from the central donor to the terminal acceptor after the photoexcitation of SMAs.[49,50] Larger relative dielectric constants (εr) for CH22 (5.45) and CH29 (5.60) could

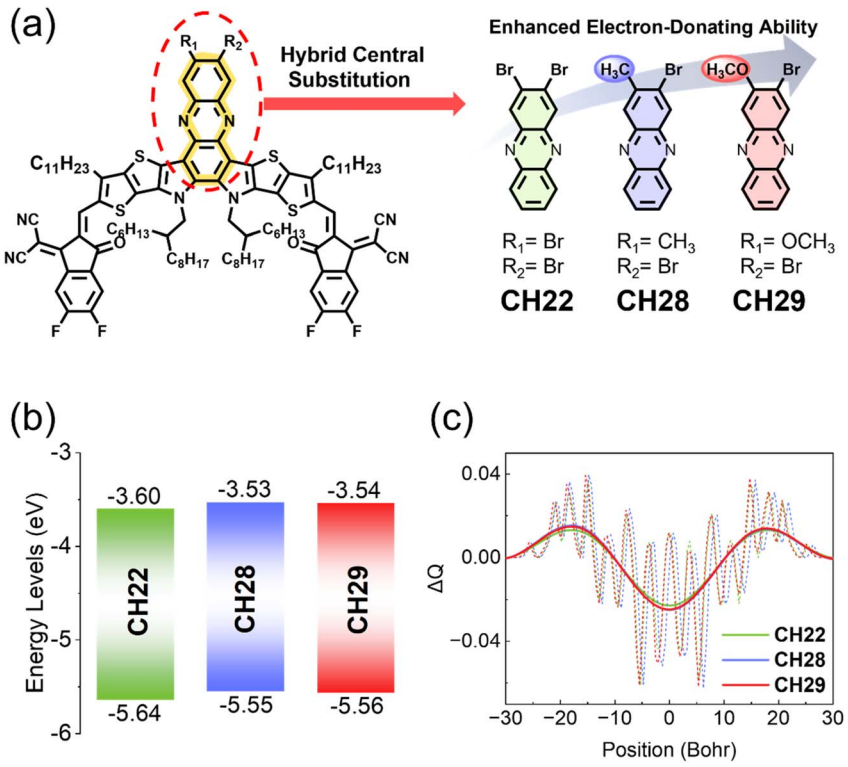

Fig. 1 (a) Chemical structures of CH22, CH28 and CH29. (b) Diagram of the theoretically calculated energy levels. (c) Theoretically calculated frontier orbital charge density differences (Δ*Q*).

be observed compared with that of CH28 (3.06) (Fig. S3†), which would be beneficial for promoting charge transfer/transport in semiconductors.[51,52]

By adopting electron-donating methyl or methoxy groups as an energy level regulator, the measured HOMOs of CH28 and CH29 (−5.64 eV), derived from cyclic voltammetry (Fig. S4 and Table S1†), showed a noticeable upshift compared with that of CH22 (−5.69 eV). This was well consistent with DFT simulations and contributed to the smaller optical bandgaps of CH28 (≈1.35 eV) and CH29 (≈1.33 eV) with respect to CH22 (≈1.39 eV), as shown in Fig. 2a. Additionally, the maximum absorption peaks of the three SMAs in films exhibited an apparent red shift compared with those in solutions, with peak wavelength changes ($\Delta\lambda$) of 83, 71 and 73 nm for CH22, CH28 and CH29, respectively (Fig. S5 and Table S2†). The decrease in $\Delta\lambda$ from CH22 to CH28/CH29 suggests a molecular packing preference variation after introducing the sterically hindered methyl or methoxy group on the central unit. Moreover, CH28 and CH29 showed slightly larger molar absorption coefficients of $\approx 1.76 \times 10^5$ L mol^{-1} cm^{-1} compared with the 1.65×10^5 L mol^{-1} cm^{-1} of CH22 (Fig. S6†). The exciton dissociation energy barriers (similar to the exciton binding energy, E_b) of CH28 and CH29 were roughly estimated to be ≈118 and 106 meV (Fig. 2b) according to the temperature-dependent PL spectra (Fig. S7†), which rank among the relatively lower categories in high-performance SMAs.[15]

To unveil the effects of hybrid central substitution on the photovoltaic properties, OSCs with a typical structure of ITO/2PACz/PM6:SMAs/PNDIT-F3N/Ag were fabricated. The chemical structure of PM6 is depicted in Fig. S8† and the device parameters under different processing conditions are summarized in Tables S3–S5.† Based on the best current density–voltage (J–V) curves and photovoltaic parameters presented in Fig. 2c and Table 1, respectively, the CH22-based binary OSC displayed an outstanding PCE of 18.84%, with a V_{OC} of 0.887 V, short-current (J_{SC}) of 26.69 mA cm^{-2}, and fill factor (FF) of 79.67%. Although the bandgap of the SMAs decreased significantly after replacing one Br atom with a methyl or methoxy group, an almost undiminished V_{OC} could be achieved, unexpectedly, especially for the CH29-based OSCs. Moreover, compared with CH22, the CH29-based OSCs possessed comparable external quantum efficiencies (EQEs) in the range of 400–800 nm; however, they also showed an obviously broadened photoelectric response (Fig. 2d), which was well consistent with the UV–vis absorption spectra of the blend films (Fig. S9†). This gave rise to a greatly improved J_{SC} of 28.30 mA

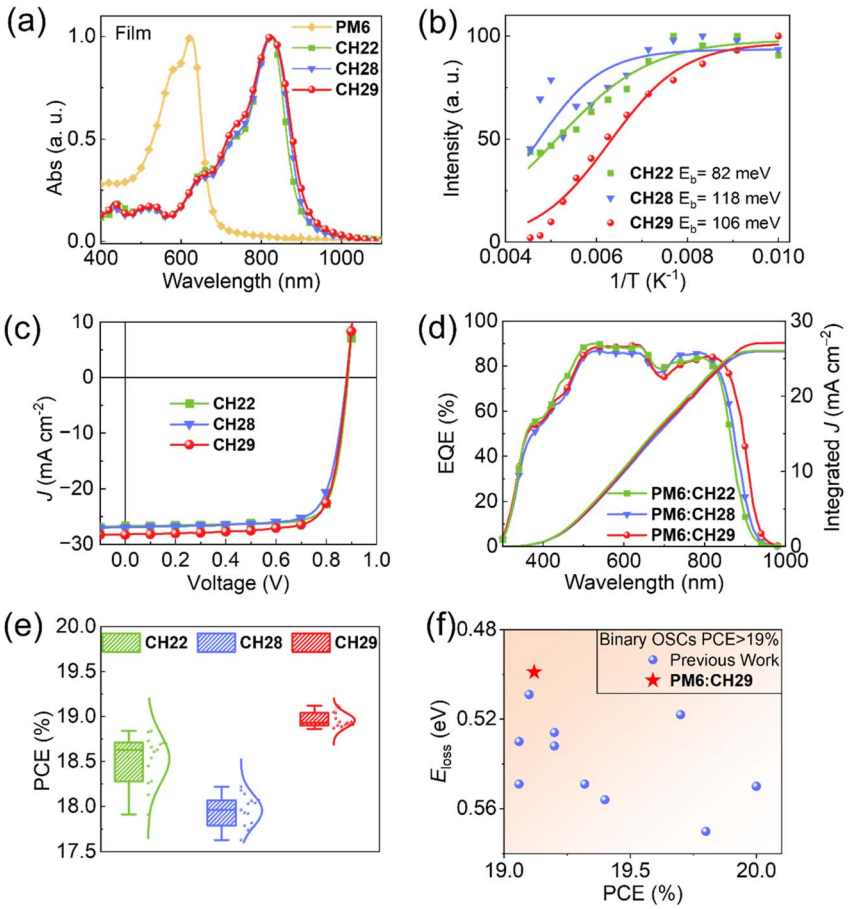

Fig. 2 (a) UV-vis absorption spectra of PM6 and the three SMAs in solid films. (b) E_b of SMAs derived from temperature-dependent photoluminescence measurements. (c) Current density–voltage curves of PM6:SMA-based OSCs. (d) EQE plots and integrated J_{SC} curves. (e) PCE variation based on 15 independent devices. (f) Statistical analysis of the energy losses on binary OSCs with efficiencies over 19%.

Table 1 Summary of the device parameters for optimized OSCs

Active layer	V_{OC} [V]	J_{SC} [mA cm^{-2}]	J_{SC}^{cal} [mA cm^{-2}]	FF [%]	PCE [%]
PM6:CH22	0.887 (0.884 ± 0.003)	26.69 (26.49 ± 0.19)	26.05	79.67 (79.15 ± 0.82)	18.84 (18.53 ± 0.27)
PM6:CH28	0.882 (0.881 ± 0.007)	26.99 (26.50 ± 0.39)	25.97	76.14 (76.84 ± 0.70)	18.22 (17.95 ± 0.18)
PM6:CH29	0.884 (0.884 ± 0.005)	28.30 (27.89 ± 0.30)	27.09	76.46 (76.98 ± 0.55)	19.12 (18.96 ± 0.08)

cm^{-2} for the CH29-based OSCs, along with an excellent and statistically improved PCE of 19.12% (Fig. 2e). The CH29-based OSCs showed a similar and even smaller optical bandgap with the classic Y6 or BTP-eC9, but rendered a significantly decreased energy loss of ≈0.499 eV. Note that this is almost the smallest energy loss reported to date in high-performance binary OSC systems with a PCE over 19% (Fig. 2f). We further carried out a detailed energy loss analysis based on the Shockley–Queisser (SQ) limit theory[53] (Fig. S10–S13†) and summarize the related parameters in Table S6.† The reduced energy loss of the CH29-based device should mainly originate from the mitigated non-radiative recombination,[54] which was experimentally supported by its larger electroluminescence external quantum efficiency (EQE_{EL}) compared with the CH22- and CH28-based devices (Fig. S9†). Additionally, the CH28- and CH29-based devices could retain over ≈80% of their initial PCE after 400 h of heat treatment at 65 °C and more than 95% after 1600 h at room temperature (Fig. S14†), indicating their good thermal tolerance and excellent long-term storage stability. These results manifest the feasibility of electron-donating and -withdrawing hybrid central substitutions for constructing high-performance NIR-OSC systems. In addition, we further explored the potential of CH28- and CH29-based devices for future commercial scale-up production, where constrains of usable solvents and allowed active layer thickness exist. As summarized in Table S7,† the PM6:CH28 and PM6:CH29 devices processed using the environmentally friendly solvent *o*-xylene achieved PCEs of 17.43% and 17.85%, respectively. Moreover, as shown in Table S8,† the PM6:CH29 device achieved a PCE of 14.79% with an active layer thickness of ≈410 nm, demonstrating potential for future commercial OSC production, where the use of green solvents and a higher thickness tolerance is essential.

It is worth noting that highly efficient photodynamic processes, including exciton dissociation, charge transport and collection (Fig. S15–S18†), were achieved by the CH28- and CH29-based OSCs, despite the significantly decreased driving forces. This should also be the prerequisite for simultaneously attaining excellent V_{OC} and J_{SC} values in CH29-based OSCs (Fig. S19†). However, an emerging drawback of CH28- and CH29-based OSCs is their inferior FFs, which decreased significantly from ≈80% to ≈76% (Table 1). These tangled and somewhat contradictory outcomes were likely due to the rebalancing of multiple photodynamic processes and were determined by the molecular packing mode and film morphology changes after introducing the electron-donating and steric methyl or methoxy groups. Therefore, CH28 and CH29 crystals were first cultivated (deposited in CCDC with numbers 2386133 for CH28; 2386134 for CH29†) and analyzed using single-crystal X-ray diffraction (XRD) measurements (Table S9 and Fig. S20 and S21†). As shown in Fig. S22,† all three SMAs exhibited helical and C-shaped molecular geometries. The N–S distance between phenazine and the connected thiophene was 3.3–3.4 Å (Fig. S22†), which was slightly shorter than the van der Waals radii addition of S and N atoms (≈3.55 Å).[55] This intramolecular non-covalent interaction could render the conjugated backbone with higher rigidity, thus resulting in a more favorable molecular packing.[15] In addition, all the SMAs formed a typical 3D molecular packing network (Fig. S23†), which has been proven to facilitate charge separation/transport while suppressing charge recombination in OSCs.[36,56,57] Notably, CH29 possessed a rectangular void with an approximate size of 15.77 × 13.89 Å, slightly smaller than that of CH22 (≈15.37 × 14.96 Å) and CH28 (≈16.66 × 14.03 Å). Moreover, CH29 had the largest molecular packing coefficient of 65.4%, compared with that of 64.3% for CH28 and 62.2% for CH22, suggesting its potentially more compact molecular packing.[58,59]

As was demonstrated in our previous work,[15,40,41,60] both the phenazine central unit and 3-(1,1-dicyanomethylene)-5,6-difluoro-1-indanone (IC-2F) terminal are deeply involved in constructing the desired 3D molecular packing network. Moreover, even a minor structural modification on phenazine may cause quite different molecular stacking modes of SMAs. Therefore, the intermolecular packing modes with intermolecular potential energies exceeding 75 kJ mol^{-1} are summarized in Fig. 3a–c and the detailed data are enumerated in Table S10.† In general, the classification of packing modes reveals that all the SMAs had a typical "E/E" mode, similar to ITIC[1] and Y-series SMAs.[47,61,62] Moreover, the unique "E/C" and dual "C/b" modes, which rarely exist in other series of SMAs, could also be afforded in the three systems. From a more microscopic perspective, their π–π stacking distance ($d_{\pi-\pi}$), intermolecular potential energy (E_{IP}), and charge-transfer integration (V_E) varied significantly due to their markedly different hyperfine molecular packing structures. To be specific, the $d_{\pi-\pi}$ decreased from CH22 (3.35 Å), CH28 (3.28 Å) to CH29 (3.16 Å) in the typical "E/E" mode, contributing to the gradually enlarged E_{IP} values from 129.9, 173.5 to 230.7 kJ mol^{-1}, respectively. Disappointingly, the DFT-calculated V_Es values of the "E/E" packings did not increase with the $d_{\pi-\pi}$s decrease, being 54.7 meV for CH22, 43.8 meV for CH28 and 19.1 meV for CH29. The decreased V_Es of the "E/E" modes will exert a negative effect on the FF of CH28- and CH29-based OSCs (Table 1). In terms of the "E/C" mode, the $d_{\pi-\pi}$ of CH28 was increased to 3.38 Å from the 3.31 Å of CH22, due to the enlarged steric hindrance on the central unit of phenazine after introducing the methyl group. Interestingly, the $d_{\pi-\pi}$ of CH29 was reduced to 3.32 Å again, which should be attributed to a newly observed intermolecular non-covalent interaction

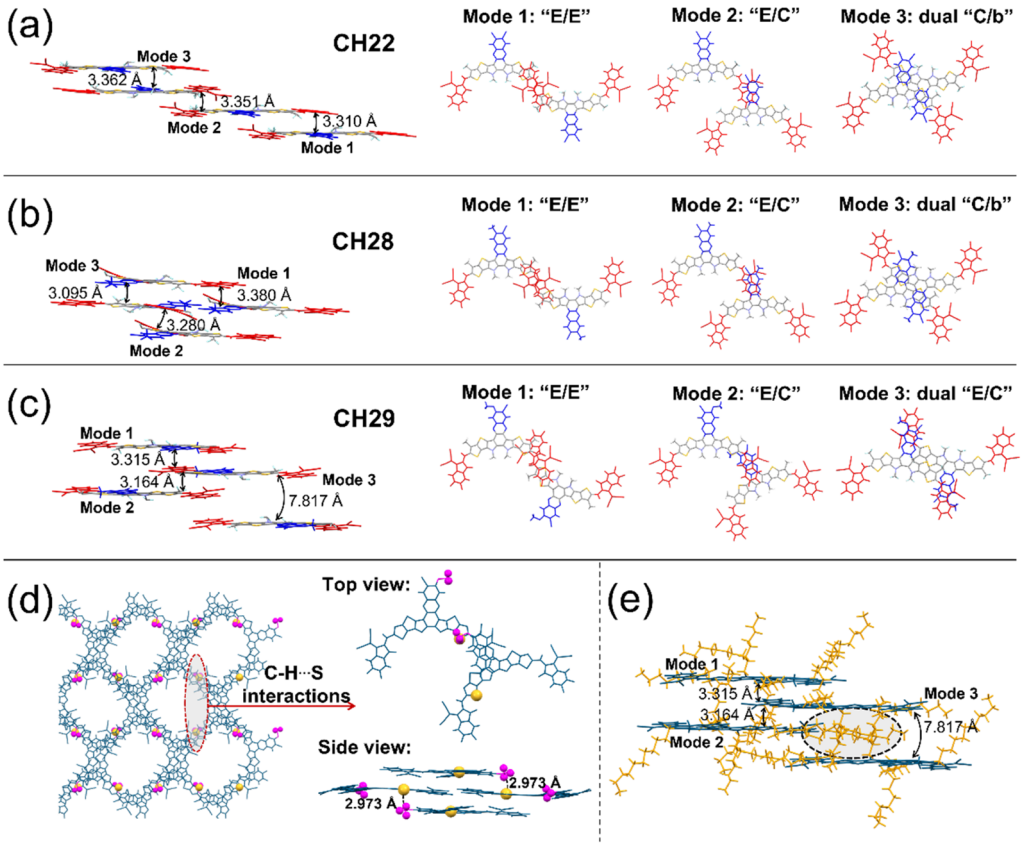

Fig. 3 Intermolecular packing modes and π–π stacking distances of (a) CH22, (b) CH28, and (c) CH29. Red, gray and blue colors mark the end "E", bridge "b" and central "C" units, respectively. (d) C–H and S non-covalent interaction existing in the CH29 crystal. (e) Dual "E/C" packing mode with a very large distance.

between the alkoxy C–H and S atom near the terminals (Fig. 3d). This non-covalent interaction was characterized by an H–S distance of 2.97 Å, which was much shorter than the sum of the van der Waals radii of H and S (≈3.09 Å).[55] However, a similar feature was not observed in the same packing mode of CH28 or other reported SMAs,[63] in spite of the existence of a methyl group (C–H) on the central unit. This inducement may originate from the unique orientation of the methoxy group caused by the large bond angle of aryl C–O–CH_3 (≈109.5°). Assisted by such a non-covalent interaction in CH29, the largest E_{IP} value of 142.2 kJ mol^{-1} and V_E of 13.6 meV among the "E/C" modes of the three SMAs were achieved. Additionally, the desirable molecular packing of CH29 facilitated achieving an electron mobility of its neat film of 7.84×10^{-4} cm^2 V^{-1} s^{-1}, compared with 6.67×10^{-4} cm^2 V^{-1} s^{-1} for CH22 and 7.84×10^{-4} cm^2 V^{-1} s^{-1} for CH28 (Table S11†). Therefore, as mentioned above, the more compact π–π packing endowed CH29 with great potential for efficient photodynamic processes, even when driven by a small driving force.

Another interesting finding was that the E_{IP} of the dual "E/C" mode in CH29 was 149.3 kJ mol^{-1}, while the $d_{\pi-\pi}$ was as large as 7.82 Å (Fig. 3e). This value is significantly larger than the typical π–π stacking distances (3.3–3.8 Å), suggesting that the strong intermolecular interaction was induced by the entanglement of alkyl chains rather than the π–π stacking of the conjugated planes. Therefore, it was reasonable to observe a very small V_E of 2.32 meV in the dual "E/C" mode of CH29. For CH22 and CH28, conventional dual "E/C" modes with relatively high π–π stacking area ratios (π–π stacking area relative to its overall molecular area) could be observed, thus rendering quite large E_{IP} values of 195.5 and 413.1 kJ mol^{-1}, respectively. Although we lack knowledge about the cause of this rare "E/C" stacking mode in the CH29 crystal or fail to directly correlate this to several specific structural elements, such an interesting finding highlights the importance of alkyl chains screening in constructing a desirable molecular stacking network, especially at the single-molecular-stacking level. This may also be one of the main reasons why plenty of side-chain engineering approaches (such as changing Y6 to L8-BO, BTP-eC9, *etc.*) can significantly regulate the molecular stacking of SMAs, in addition to the optimization of conjugated backbones.

To sum up, after introducing a steric methyl and methoxy group on the phenazine central unit, the average $d_{\pi-\pi}$ showed an unexpected decrease from CH22 to CH29, especially for the typical "E/E" packing mode. However, the obviously reduced $d_{\pi-\pi}$ did not lead to improved V_E values for CH28 and CH29, which may partially account for their inferior FFs compared with that of CH22. In addition, a distinctive non-covalent interaction between the alkoxy C–H and S atom existed in the "E/C" mode of CH29, contributing to its largest E_{IP} of 142.9 kJ mol^{-1} and V_E of

13.6 meV among the "E/C" modes of all three SMAs. This unveils the great capacity of methoxy groups to enhance the intermolecular interactions of SMAs by forming desirable non-covalent bonds. Finally, for the first time, an unconventional "E/C" stacking mode in CH29, featuring a relatively large E_{IP} due to the entanglement of alkyl chains rather than the π–π stacking of conjugated planes, was revealed and discussed. This may help explain the underlying reason why the side-chain engineering of SMAs could successfully regulate the molecular stacking of SMAs, further providing a guideline for designing SMAs with better photovoltaic outcomes.

Single-crystal analysis could reflect the molecular packing properties to some extent. However, a bias always exists owing to the significantly different crystallization rates between single-crystal cultivation and film formation.[45] As displayed in Fig. 4b, which presents the grazing incidence wide angle X-ray scattering (GIWAXS) line-cut profiles of neat films, and the detailed data summarized in Table S12,† CH22, CH28 and CH29 exhibited obvious (010) diffraction peaks located at 1.61, 1.63 and 1.65 $Å^{-1}$ in the OOP direction and sharp (100) diffraction peaks at 0.271, 0.290, 0.288 $Å^{-1}$ in the IP direction, respectively. This demonstrates that all three SMAs had a preferential face-on orientation on silicon substrates. Notably, CH29 showed a (010) diffraction peak that was slightly shifted to the higher q region, resulting from a smaller π–π stacking distance of 3.81 Å compared with 3.90 Å for CH22 and 3.85 Å for CH28, which roughly aligned with the analysis of the single crystals. In addition, a comparable but slightly larger crystal coherence length (CCL) of 17.7 Å could be observed for the CH29 neat film compared with 16.4 Å for CH22 and 16.9 Å for CH28 in the OOP directions, indicating its enhanced molecular π–π stacking order. Note that the packing modes of the three SMAs were observed to be well preserved in the spin-coated films. Taking CH29 as an example, the X-ray diffraction (XRD) pattern simulated from the single-crystal structure (Fig. S24†) displayed strong peaks at 0.357, 0.508 and 1.723 $Å^{-1}$, corresponding to packing distances of 17.58, 12.37, 3.65 Å, respectively, which was well consistent with the GIWAXS data of the CH29 neat film. Alternatively, CH22 afforded a greatly enlarged CCL of 73.4 Å in the IP direction compared with 52.4 Å for CH28 and 58.3 Å for CH29. Such a long-range order in the CH22 film may account for the excellent FFs of OSCs.[64] After blending with the

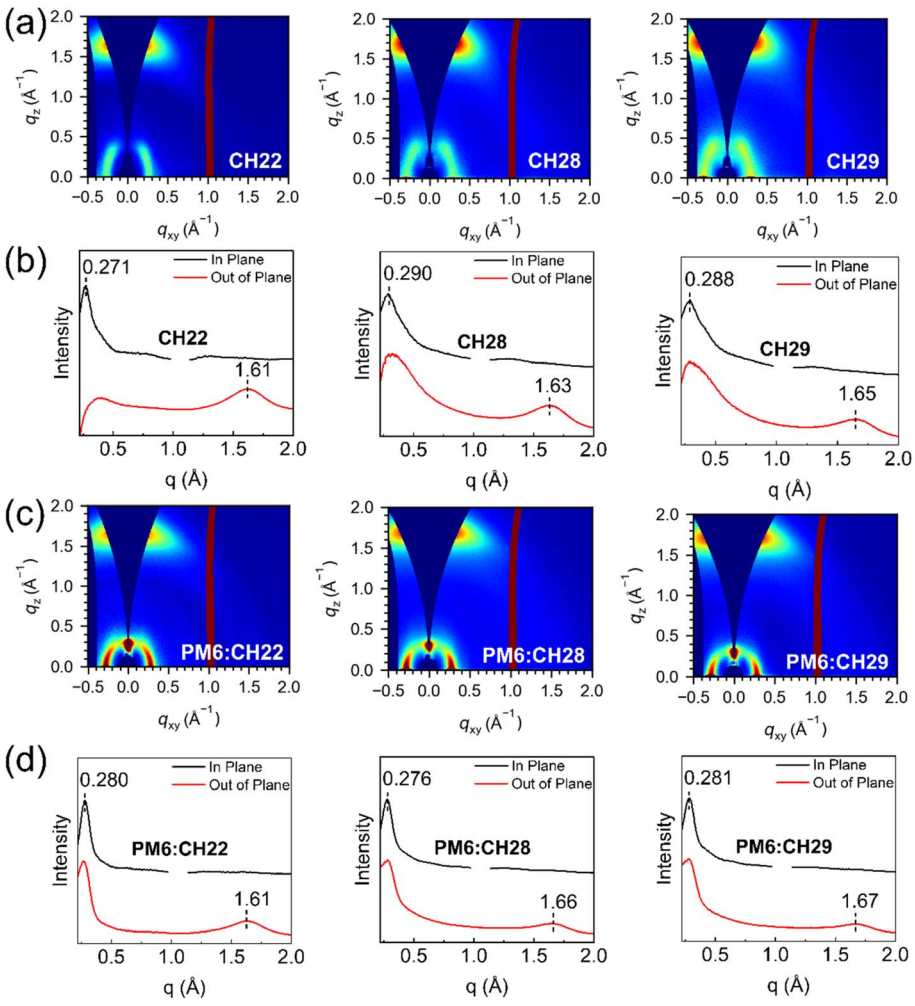

Fig. 4 (a and c) 2D GIWAXS patterns of neat films of SMAs and blended films of PM6:SMAs. (b and d) Corresponding in-plane (IP) and out-of-plane (OOP) extracted line-cut profiles of neat films of SMAs and blended films of PM6:SMAs.

PM6 donor, a similar tendency could also be observed (Fig. 4d), suggesting that the molecular packing features could be well maintained.

The morphology of blended films of PM6:SMAs at the nanoscale will largely determine the photovoltaic performance of OSCs. Therefore, atomic force microscopy (AFM) was employed to examine the surficial morphology of the blended films. As shown in Fig. S25,† all the blends exhibited a smooth surface, as indicated by a root-mean-square (RMS) roughness of ≈0.8 nm. As for the phase images (Fig. S26†), a fibrillary morphology could be clearly observed in PM6:CH22 and PM6:CH29, which has been regarded as one of the prerequisites for efficient charge transport in OSCs.[65]

AFM coupled infrared spectroscopy (AFM-IR) allows for the rough distinction of donor and acceptor domains by monitoring the characteristic IR peak at ≈2216 cm^{-1} of acceptors, and thereby can provide a more detailed landscape of D/A blended films.[66] As presented in Fig. 5a, both the CH22 and CH29 blends displayed pronounced fibril D/A interpenetrating networks, especially CH22. Moreover, the average D/A fibril diameters were statistically estimated (Fig. S27†) and are shown in Fig. 5b, being ≈12.3 nm for PM6:CH22, ≈10.3 nm for PM6:CH28 and ≈10.7 nm for PM6:CH29. Subsequently, *in situ* UV–vis absorption measurements were conducted to unveil the molecular crystallization dynamics during film formation (Fig. 5c and S29†). When thermal annealing starts, the stacking molecules will transform from a metastable state to a relatively stable one through molecular movement and rearrangements,[67] typically causing an obvious redshift of the absorption peaks. As indicated in Fig. 5d, the CH22 blends could reach a stable state within ≈1.2 s, faster than the CH28 (1.8 s) and CH29 (1.4 s) blends. These results indicate that Br atoms on the central unit could effectively promote molecular rearrangement and induce a relatively larger phase separation, which should be

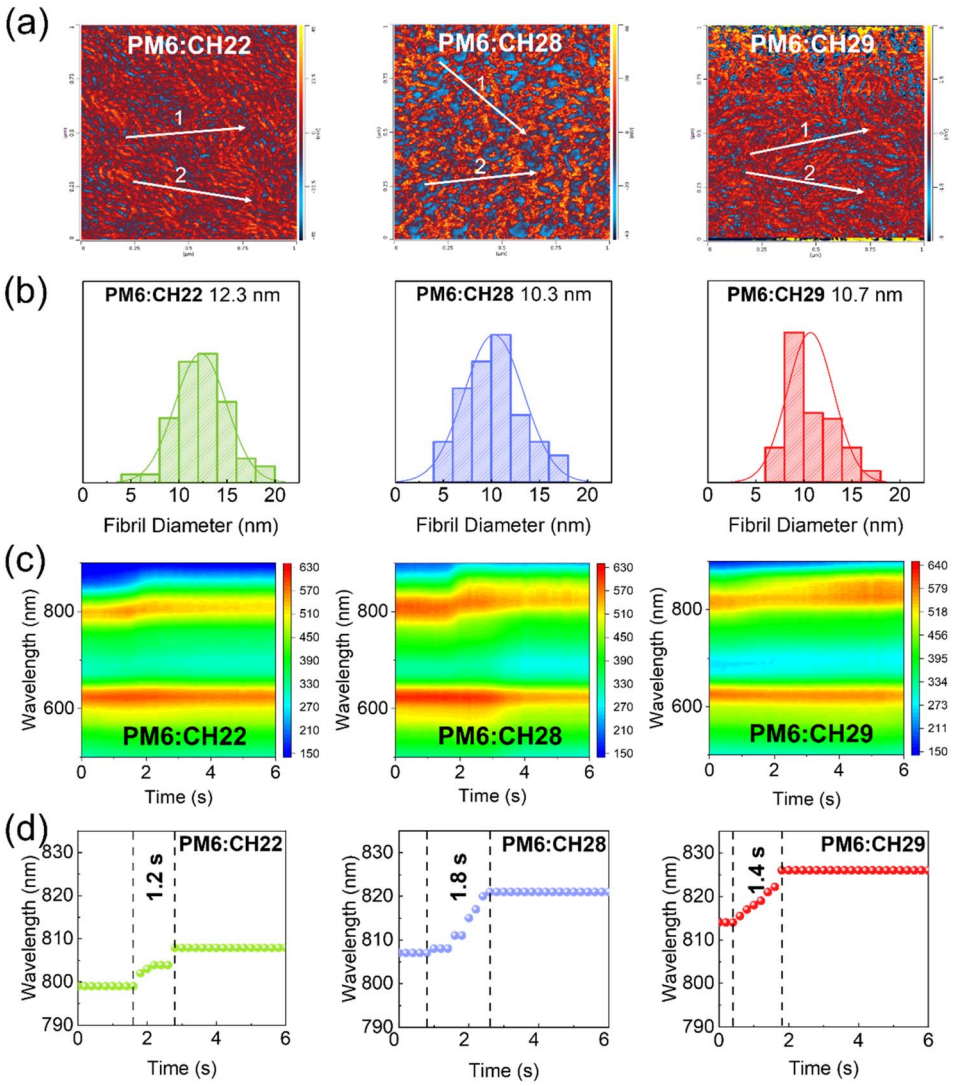

Fig. 5 (a) AFM-IR phase images of the blended films. The donor and acceptor domains are distinguished by blue and red colors, respectively. (b) Statistical distribution of phase-separation sizes. (c) Color mapping of *in situ* UV–vis absorption spectra. (d) Absorption peak wavelength evolution.

responsible for the superior FF of over 80% in the CH22-based OSCs. Notably, compared with CH28, the favorable fibrillary morphology could still be maintained in the CH29 films. This may benefit from the enhanced intermolecular interactions of CH29, caused by the non-covalent bond of OC-H···S. In short, by employing central hybrid substitution and careful substituted groups screening, CH29 achieved a delicate but superior balance between high molecular crystallization and redshifted absorption, thereby allowing developing highly efficient NIR-OSCs at last.

Conclusion

With the aim of boosting the absorption of SMAs to the NIR region while simultaneously maintaining their favorable molecular packing, we developed a synergistic strategy of hybrid central substitution on 2D conjugation-extended SMAs. To be specific, on the basis of the high-performance molecular skeleton of CH22, a moderate or strong electron-donating group (methyl or methoxy) was incorporated into one active site of the central unit, thus leaving another position for inclusion of the bromine atom to promote ordered molecular packing. By taking full advantage of the strong electron-rich methoxy group and high crystallinity of bromine whilst compensating for the emerged steric-hindrance on central units, a CH29-based OSC achieved a quite narrow optical bandgap of $\approx$1.33 eV (similar to the classic BTP-eC9) but a really high V_{OC} of 884 mV, thus offering one of the lowest energy losses thus far reported for high-performance OSC systems. A detailed crystal analysis of CH29 revealed that (1) the rarely observed OC–H···S non-covalent interaction existed in the "E/C" packing mode, which enhanced π–π stacking interactions; (2) in addition to π–π stacking, the entanglement of alkyl chains gave rise to a strong long-range (over 7 Å) intermolecular interaction, which can potentially shed light on the underlying reason at the single molecular level as to why side-chain engineering could successfully regulate the molecular stacking of the SMAs. Benefiting from the above factors, the PM6:CH29 blend maintained a fibrillary morphology similar to that of PM6:CH22 in spite of the larger steric hindrance on the central unit of CH29. Finally, CH29 achieved a superior balance between high molecular crystallinity and redshifted absorption, thus rendering highly efficient NIR-OSCs with a PCE of 19.12%. Our work developed a feasible strategy of hybrid central substitution for constructing high-performance NIR-SMAs and should certainly stimulate unremitting trials on this strategy, such as utilizing more electron-rich amine-based groups to replace the methoxy group.

Data availability

The data that support the findings of this study are available from the corresponding author upon reasonable request.

Author contributions

The synthetic works were carried out by Y. L. and X. B.; the device optimizations and measurements were carried out by X. J.; K. W. and Z. Z. performed the single-crystal measurements and analysis. W. Z. and G. L. performed the DFT calculations. Y. Z. and Y. C. directed the study and revised the manuscript. X. C., Y. G., C. L., and X. W. helped analyze the data and commented on the manuscript.

Conflicts of interest

The authors declare no competing financial interest.

Acknowledgements

The authors gratefully acknowledge the financial support from Ministry of Science and Technology of the People's Republic of China (National Key R&D Program of China, 2022YFB4200400), National Natural Science Foundation of China (21935007, 52025033, 51873089, 22204119, 22309090, 22474089, 22479081), Natural Science Foundation of Tianjin (23JCZDJC00140) and Haihe Laboratory of Sustainable Chemical Transformations.

References

1 Y. Lin, J. Wang, Z.-G. Zhang, H. Bai, Y. Li, D. Zhu and X. Zhan, *Adv. Mater.*, 2015, **27**, 1170–1174.
2 J. Yuan, Y. Zhang, L. Zhou, G. Zhang, H.-L. Yip, T.-K. Lau, X. Lu, C. Zhu, H. Peng, P. A. Johnson, M. Leclerc, Y. Cao, J. Ulanski, Y. Li and Y. Zou, *Joule*, 2019, **3**, 1140–1151.
3 G. Yu, J. Gao, J. C. Hummelen, F. Wudl and A. J. Heeger, *Science*, 1995, **270**, 1789–1791.
4 F. Lin, K. Jiang, W. Kaminsky, Z. Zhu and A. K. Y. Jen, *J. Am. Chem. Soc.*, 2020, **142**, 15246–15251.
5 Z. Jia, S. Qin, L. Meng, Q. Ma, I. Angunawela, J. Zhang, X. Li, Y. He, W. Lai, N. Li, H. Ade, C. J. Brabec and Y. Li, *Nat. Commun.*, 2021, **12**, 178.
6 Y. Liu and T. P. Russell, *Acc. Chem. Res.*, 2022, **55**, 1097–1108.
7 C. Chen, L. Wang, W. Xia, K. Qiu, C. Guo, Z. Gan, J. Zhou, Y. Sun, D. Liu, W. Li and T. Wang, *Nat. Commun.*, 2024, **15**, 6865.
8 Z. Chen, J. Ge, W. Song, X. Tong, H. Liu, X. Yu, J. Li, J. Shi, L. Xie, C. Han, Q. Liu and Z. Ge, *Adv. Mater.*, 2024, **36**, 2406690.
9 Y. Jiang, S. Sun, R. Xu, F. Liu, X. Miao, G. Ran, K. Liu, Y. Yi, W. Zhang and X. Zhu, *Nat. Energy*, 2024, **9**, 975–986.
10 Y. Sun, L. Wang, C. Guo, J. Xiao, C. Liu, C. Chen, W. Xia, Z. Gan, J. Cheng, J. Zhou, Z. Chen, J. Zhou, D. Liu, T. Wang and W. Li, *J. Am. Chem. Soc.*, 2024, **146**, 12011–12019.
11 L. Zhu, M. Zhang, G. Zhou, Z. Wang, W. Zhong, J. Zhuang, Z. Zhou, X. Gao, L. Kan, B. Hao, F. Han, R. Zeng, X. Xue, S. Xu, H. Jing, B. Xiao, H. Zhu, Y. Zhang and F. Liu, *Joule*, 2024, **8**(11), 3153–3168.
12 N. Wei, J. Chen, Y. Cheng, Z. Bian, W. Liu, H. Song, Y. Guo, W. Zhang, Y. Liu, H. Lu, J. Zhou and Z. Bo, *Adv. Mater.*, 2024, **36**, 2408934.
13 C. Li, G. Yao, X. Gu, J. Lv, Y. Hou, Q. Lin, N. Yu, M. S. Abbasi, X. Zhang, J. Zhang, Z. Tang, Q. Peng, C. Zhang, Y. Cai and H. Huang, *Nat. Commun.*, 2024, **15**, 8872.

14 H. Chen, Y. Zou, H. Liang, T. He, X. Xu, Y. Zhang, Z. Ma, J. Wang, M. Zhang, Q. Li, C. Li, G. Long, X. Wan, Z. Yao and Y. Chen, *Sci. China: Chem.*, 2022, **65**, 1362–1373.
15 H. Liang, X. Bi, H. Chen, T. He, Y. Lin, Y. Zhang, K. Ma, W. Feng, Z. Ma, G. Long, C. Li, B. Kan, H. Zhang, O. A. Rakitin, X. Wan, Z. Yao and Y. Chen, *Nat. Commun.*, 2023, **14**, 4707.
16 H. Liang, H. Chen, P. Wang, Y. Zhu, Y. Zhang, W. Feng, K. Ma, Y. Lin, Z. Ma, G. Long, C. Li, B. Kan, Z. Yao, H. Zhang, X. Wan and Y. Chen, *Adv. Funct. Mater.*, 2023, **33**, 2301573.
17 W. Liu, H. Yu, B. Liu, Y. Wang, H. Hu, H. M. Ng, C. H. Kwok, J. Yi, C. Zhang, F. Huang, Z. Zhu and H. Yan, *Adv. Funct. Mater.*, 2024, **34**, 2400131.
18 Q. Wei, S. Liang, W. Liu, Y. Hu, B. Qiu, J. Ren, J. Yuan, F. Huang, Y. Zou and Y. Li, *ACS Energy Lett.*, 2022, **7**, 2373–2381.
19 Y. Zhang, J. Chen, J. Yang, M. Fu, Y. Cao, M. Dong, J. Yu, S. Dong, X. Yang, L. Shao, Z. Hu, H. Cai, C. Liu and F. Huang, *Adv. Mater.*, 2024, **36**, 2406950.
20 R. Englman and J. Jortner, *Mol. Phys.*, 1970, **18**, 145–164.
21 J. Benduhn, K. Tvingstedt, F. Piersimoni, S. Ullbrich, Y. Fan, M. Tropiano, K. A. McGarry, O. Zeika, M. K. Riede, C. J. Douglas, S. Barlow, S. R. Marder, D. Neher, D. Spoltore and K. Vandewal, *Nat. Energy*, 2017, **2**, 17053.
22 M. Bixon, J. Jortner, J. Cortes, H. Heitele and M. E. Michel-Beyerle, *J. Phys. Chem.*, 1994, **98**, 7289–7299.
23 Y. Dong, H. Cha, H. L. Bristow, J. Lee, A. Kumar, P. S. Tuladhar, I. McCulloch, A. A. Bakulin and J. R. Durrant, *J. Am. Chem. Soc.*, 2021, **143**, 7599–7603.
24 N. A. Ran, J. A. Love, C. J. Takacs, A. Sadhanala, J. K. Beavers, S. D. Collins, Y. Huang, M. Wang, R. H. Friend, G. C. Bazan and T.-Q. Nguyen, *Adv. Mater.*, 2016, **28**, 1482–1488.
25 G. Han and Y. Yi, *J. Phys. Chem. Lett.*, 2019, **10**, 2911–2918.
26 F. D. Eisner, M. Azzouzi, Z. Fei, X. Hou, T. D. Anthopoulos, T. J. S. Dennis, M. Heeney and J. Nelson, *J. Am. Chem. Soc.*, 2019, **141**, 6362–6374.
27 M. A. Green, *Prog. Photovoltaics*, 2012, **20**, 472–476.
28 G. Dennler, M. C. Scharber, T. Ameri, P. Denk, K. Forberich, C. Waldauf and C. J. Brabec, *Adv. Mater.*, 2008, **20**, 579–583.
29 A. Hadipour, B. de Boer and P. W. M. Blom, *Adv. Funct. Mater.*, 2008, **18**, 169–181.
30 S. Sista, Z. Hong, L.-M. Chen and Y. Yang, *Energy Environ. Sci.*, 2011, **4**, 1606–1620.
31 L. Yang, H. Zhou, S. C. Price and W. You, *J. Am. Chem. Soc.*, 2012, **134**, 5432–5435.
32 O. Adebanjo, P. P. Maharjan, P. Adhikary, M. Wang, S. Yang and Q. Qiao, *Energy Environ. Sci.*, 2013, **6**, 3150–3170.
33 T. Ameri, N. Li and C. J. Brabec, *Energy Environ. Sci.*, 2013, **6**, 2390–2413.
34 S. Lu, X. Guan, X. Li, W. E. I. Sha, F. Xie, H. Liu, J. Wang, F. Huang and W. C. H. Choy, *Adv. Energy Mater.*, 2015, **5**, 1500631.
35 L. Zuo, X. Shi, S. B. Jo, Y. Liu, F. Lin and A. K.-Y. Jen, *Adv. Mater.*, 2018, **30**, 1706816.
36 W. Zhu, A. P. Spencer, S. Mukherjee, J. M. Alzola, V. K. Sangwan, S. H. Amsterdam, S. M. Swick, L. O. Jones, M. C. Heiber, A. A. Herzing, G. Li, C. L. Stern, D. M. DeLongchamp, K. L. Kohlstedt, M. C. Hersam, G. C. Schatz, M. R. Wasielewski, L. X. Chen, A. Facchetti and T. J. Marks, *J. Am. Chem. Soc.*, 2020, **142**, 14532–14547.
37 C. Lin, T. Kim, J. D. Schultz, R. M. Young and M. R. Wasielewski, *Nat. Chem.*, 2022, **14**, 786–793.
38 Y.-C. Wei, S. F. Wang, Y. Hu, L.-S. Liao, D.-G. Chen, K.-H. Chang, C.-W. Wang, S.-H. Liu, W.-H. Chan, J.-L. Liao, W.-Y. Hung, T.-H. Wang, P.-T. Chen, H.-F. Hsu, Y. Chi and P.-T. Chou, *Nat. Photonics*, 2020, **14**, 570–577.
39 H. Chen, H. Liang, Z. Guo, Y. Zhu, Z. Zhang, Z. Li, X. Cao, H. Wang, W. Feng, Y. Zou, L. Meng, X. Xu, K. Bin, C. Li, Z. Yao, X. Wan, Z. Ma and Y. Chen, *Angew. Chem., Int. Ed.*, 2022, **61**, e202209580.
40 H. Liang, H. Chen, P. Wang, Y. Zhu, Y. Zhang, W. Feng, K. Ma, Y. Lin, Z. Ma, G. Long, C. Li, B. Kan, Z. Yao, H. Zhang, X. Wan and Y. Chen, *Adv. Funct. Mater.*, 2023, **33**, 2301573.
41 Z. Yao, X. Cao, X. Bi, T. He, Y. Li, X. Jia, H. Liang, Y. Guo, G. Long, B. Kan, C. Li, X. Wan and Y. Chen, *Angew. Chem., Int. Ed.*, 2023, **62**, e202312630.
42 Y. Zou, H. Chen, X. Bi, X. Xu, H. Wang, M. Lin, Z. Ma, M. Zhang, C. Li, X. Wan, G. Long, Y. Zhaoyang and Y. Chen, *Energy Environ. Sci.*, 2022, **15**, 3519–3533.
43 R. Sun, Y. Wu, X. R. Yang, Y. Gao, Z. Chen, K. Li, J. W. Qiao, T. Wang, J. Guo, C. Liu, X. T. Hao, H. M. Zhu and J. Min, *Adv. Mater.*, 2022, **34**, 11.
44 L. Meng, Y. Zhang, X. Wan, C. Li, X. Zhang, Y. Wang, X. Ke, Z. Xiao, L. Ding, R. Xia, H.-L. Yip, Y. Cao and Y. Chen, *Science*, 2018, **361**, 1094–1098.
45 G. Zhang, X.-K. Chen, J. Xiao, P. C. Y. Chow, M. Ren, G. Kupgan, X. Jiao, C. C. S. Chan, X. Du, R. Xia, Z. Chen, J. Yuan, Y. Zhang, S. Zhang, Y. Liu, Y. Zou, H. Yan, K. S. Wong, V. Coropceanu, N. Li, C. J. Brabec, J.-L. Bredas, H.-L. Yip and Y. Cao, *Nat. Commun.*, 2020, **11**, 3943.
46 F. Zhao, S. Dai, Y. Wu, Q. Zhang, J. Wang, L. Jiang, Q. Ling, Z. Wei, W. Ma, W. You, C. Wang and X. Zhan, *Adv. Mater.*, 2017, **29**, 1700144.
47 Z. Bi, K. Chen, L. Gou, Y. Guo, X. Zhou, H. B. Naveed, J. Wang, Q. Zhu, J. Yuan, C. Zhao, K. Zhou, S. Chandrabose, Z. Tang, Y. Yi, J. M. Hodgkiss, L. Zhang and W. Ma, *J. Mater. Chem. A*, 2021, **9**, 16733–16742.
48 G. Han, Y. Guo, X. Song, Y. Wang and Y. Yi, *J. Mater. Chem. C*, 2017, **5**, 4852–4857.
49 B. S. Rolczynski, J. M. Szarko, H. J. Son, Y. Liang, L. Yu and L. X. Chen, *J. Am. Chem. Soc.*, 2012, **134**, 4142–4152.
50 R. Tautz, E. Da Como, T. Limmer, J. Feldmann, H.-J. Egelhaaf, E. von Hauff, V. Lemaur, D. Beljonne, S. Yilmaz, I. Dumsch, S. Allard and U. Scherf, *Nat. Commun.*, 2012, **3**, 970.
51 Z. Fu, X. Zhang, H. Zhang, Y. Li, H. Zhou and Y. Zhang, *Chin. J. Chem.*, 2021, **39**, 381–390.
52 W. Jiang, H. Jin, M. Babazadeh, A. S. Loch, A. Raynor, N. Mallo, D. M. Huang, X. Jiao, W. L. Tan, C. R. McNeill, P. L. Burn and P. E. Shaw, *Adv. Funct. Mater.*, 2022, **32**, 2104259.

53 W. Shockley and H. J. Queisser, *J. Appl. Phys.*, 1961, **32**, 510–519.
54 X.-K. Chen, D. Qian, Y. Wang, T. Kirchartz, W. Tress, H. Yao, J. Yuan, M. Huelsbeck, M. Zhang, Y. Zou, Y. Sun, Y. Li, J. Hou, O. Inganas, V. Coropceanu, J.-L. Bredas and F. Gao, *Nat. Energy*, 2021, **6**, 799–806.
55 P. Politzer and J. S. Murray, *Struct. Chem.*, 2021, **32**, 623–629.
56 Z. Yao, X. Wan, C. Li and Y. Chen, *Acc. Mater. Res.*, 2023, **4**, 772–785.
57 C. Li, J. Zhou, J. Song, J. Xu, H. Zhang, X. Zhang, J. Guo, L. Zhu, D. Wei, G. Han, J. Min, Y. Zhang, Z. Xie, Y. Yi, H. Yan, F. Gao, F. Liu and Y. Sun, *Nat. Energy*, 2021, **6**, 605–613.
58 Y. Li, J. Song, Y. Dong, H. Jin, J. Xin, S. Wang, Y. Cai, L. Jiang, W. Ma, Z. Tang and Y. Sun, *Adv. Mater.*, 2022, **34**, 2110155.
59 J. Cai, Y. Fu, C. Guo, D. Li, L. Wang, C. Chen, D. Liu, W. Li and T. Wang, *Sci. China: Chem.*, 2023, **66**, 508–517.
60 X. Bi, X. Cao, T. He, H. Liang, Z. Yao, J. Yang, Y. Guo, G. Long, B. Kan, C. Li, X. Wan and Y. Chen, *Small*, 2024, **20**, 2401054.
61 K. Sun, Z. Xiao, S. Lu, W. Zajaczkowski, W. Pisula, E. Hanssen, J. M. White, R. M. Williamson, J. Subbiah, J. Ouyang, A. B. Holmes, W. W. H. Wong and D. J. Jones, *Nat. Commun.*, 2015, **6**, 6013.
62 H. Yao, Y. Cui, R. Yu, B. Gao, H. Zhang and J. Hou, *Angew. Chem., Int. Ed.*, 2017, **56**, 3045–3049.
63 Y. Gong, T. Zou, X. Li, S. Qin, G. Sun, T. Liang, R. Zhou, J. Zhang, J. Zhang, L. Meng, Z. Wei and Y. Li, *Energy Environ. Sci.*, 2024, **17**, 6844–6855.
64 M. Más-Montoya and R. A. J. Janssen, *Adv. Funct. Mater.*, 2017, **27**, 1605779.
65 S. Li, L. Zhan, N. Yao, X. Xia, Z. Chen, W. Yang, C. He, L. Zuo, M. Shi, H. Zhu, X. Lu, F. Zhang and H. Chen, *Nat. Commun.*, 2021, **12**, 4627.
66 A. Dazzi and C. B. Prater, *Chem. Rev.*, 2017, **117**, 5146–5173.
67 Z. Shen, J. Yu, G. Lu, K. Wu, Q. Wang, L. Bu, X. Liu, Y. Zhu and G. Lu, *Energy Environ. Sci.*, 2023, **16**, 2945–2956.

